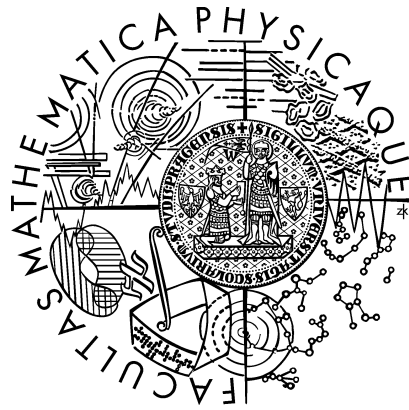CHARLES UNIVERSITY IN PRAGUE
FACULTY OF MATHEMATICS AND PHYSICS

DIPLOMA THESIS

Viktor Pěč

Background effects in neutrino oscillation measurement

INSTITUTE OF PARTICLE AND NUCLEAR PHYSICS

Supervisor: Ing. Vít Vorobel, Ph.D.
Study programme: Physics
Study field: Nuclear and Subnuclear Physics

I would like to thank to my supervisor Vít Vorobel for leading me in the work, for his advice and introduction to the problem. Many thanks belong to members of Daya Bay collaboration, especially to Haoqi Lu, who provided his experience to me during my stay in Beijing.

Finally I'm very grateful to many members and students of Institute of Particle and Nuclear Physics MFF UK for help and leading through the three years of my studies at the institute.

Prohlašuji, že jsem svou diplomovou práci napsal samostantně a výhradně s použitím citovaných pramenů. Souhlasím se zapůjčováním práce.

I declare that I wrote my diploma thesis independently and exclusively with the use of the cited sources. I agree with lending the thesis.

Prague, 8th August 2007   Viktor Pěč

List of Figures

List of Tables

Contents

Název práce: Efekty pozadí v měření oscilací neutrin

Autor: Viktor Pěč

Katedra (ústav): Ústav částicové a jaderné fyziky

Vedoucí diplomové práce: Ing. Vít Vorobel, Ph.D.

e-mail vedoucího: vorobel@ipnp.troja.mff.cuni.cz

Abstrakt: Práce je zaměřena na simulaci pozadí v neutrinovém experimentu Daya Bay. Jedná se o odhad příspěvku procesu, kdy dojde k emisi neutronu po záchytu kosmického mionu na jádře kyslíku v okolí detektoru. Proces byl studován pomocí Monte Carlo metody s využitím simulačního nástroje Geant4 a balíčku G4dyb, vyvíjeného v rámci kolaborace Daya Bay. Simulace byla provedena pro vzdálený detektor a byla rozdělena na dvě části. V první byly simulovány "neviditelné" záporné miony, kde neviditelnost byla dána produkcí méně než 1000 čerenkovských fotonů ve vodním čerenkovském detektoru. V druhé části byly simulovány neutrony vzniklé při mionovém záchytu. Z celkového počtu 3.3 miliardy mionů, 458 tisíc jich bylo zachyceno ve vodním bazéně s následnou produkcí neutronu. Pouze 10 neutronů se dostalo až do hlavního detektoru a bylo zachyceno jádrem gadolinia. Uvedené počty odpovídají 1700 let reálného času. Takto ohromné číslo je důsledkem použití vodního stínění a odráží fakt, jak důležité je takové stínění pro potlačení neutronového pozadí. Výsledek vypovídá o zanedbatelnosti pozadí způsobeného mionovým záchytem.

Klíčová slova: oscilace neutrin, pozadí, Geant4, experiment Daya Bay

Title: Background effects in neutrino oscillation measurement

Author: Viktor Pěč

Department: Institute of Particle and Nuclear Physics

Supervisor: Ing. Vít Vorobel, Ph.D.

Supervisor's e-mail address: vorobel@ipnp.troja.mff.cuni.cz

Abstract: The goal of this diploma thesis is to present results of Monte Carlo simulations of cosmic muon capture induced neutron background for the Daya Bay reactor neutrino experiment. For this purpose, program package G4dyb, which is based on the Geant4 software toolkit and developed by Daya Bay collaboration members, was used to perform simulations for detector at "far site". The work was partitioned into two parts, simulation of muons in the detector's water pool and simulation of consequently emitted neutrons. Only "visible" muons were taken into account. The visibility was defined by restriction on muons which produce less than 1000 Cherenkov photons in the water pool. From 3.3 billion of muons, 458 thousands μ^- were captured with neutron emission in the water pool. Only 10 neutrons got into the anti-neutrino module and captured on gadolinium. The corresponding time is roughly 1700 years. Such a low rate is a consequence of the water shield presence and reflects the fact how important is the water shielding for neutron background suppression. The result shows that this type of background is negligible.

Keywords: neutrinos oscillation, background, Geant4, Daya Bay experiment

1 Introduction

Since the observation of neutrino oscillations has unequivocally demonstrated that the masses of neutrinos are nonzero, the Standard Model of particle physics appeared to be incomplete. Many kinds of experiments accomplished measurements and few parameters of the oscillations are known nowadays, however, there is still open field for further exploration.

The Daya Bay reactor neutrino experiment is aimed to measure the last unknown mixing angle θ_{13} which is very small or vanishing. To achieve a high sensitivity one of the most powerful nuclear power plants, the Daya Bay nuclear power complex, is exploited as a prolific sources of electron anti-neutrinos.

The goal of this diploma thesis is to present results of Monte Carlo simulations of particular background type, neutrons from muon capture in the vicinity of the detector. The program package G4dyb, which is based on the Geant4 software toolkit and developed by Daya Bay collaboration members, was used to perform such simulations.

The first part of the thesis provides a brief introduction into the neutrino oscillations phenomenology. Current knowledge and experiments involved into this topic are reviewed. The third section presents design of the Daya Bay experiment and outlines the expected backgrounds, along with description of muon capture. The second part describes the work, which has been done to estimate rate of neutrons from the muon capture. Some comparison of partial results is presented. The appendix provides additional information on MC simulations, Cherenkov radiation, and photo-multiplier tubes.

2 Neutrino oscillation phenomenology

Compelling evidence of transformation of one neutrino flavor to another—neutrino oscillations—has been observed in solar, atmospheric, reactor and accelerator experiments, using a wide variety of detector technologies. The only known consistent explanation of these results is that neutrinos have a mass and that the mass eigenstates are not the same as the flavor eigenstates—this is called neutrino mixing.

This section provides a kind of basic insight into the phenomenology of the neutrino mixing and oscillations. Fundamental parameters of this phenomenology are introduced in following subsections, together with basic review of the current knowledge and of the past, present, and proposed experiments involved in this phenomena.

2.1 Neutrino mixing

Assuming that flavor eigenstates are not the same as the mass ones, there exists unitary transformation U which transforms one basis into another. Denoting mass eigenstates with latin and flavor eigenstates with greek symbols, the transformation can be expressed by

$$|\nu_i\rangle = U_{\alpha i}|\nu_\alpha\rangle, \tag{1}$$

where the standard Einstein's summation convention—the right-hand side is summed over the doubled indexes, α in this case—was used, as well as the usual bra-ket notation. The matrix $U_{\alpha i}$ is usually called mixing matrix and from eq. (1) it's elements are as follows

$$U_{\alpha i} = \langle \nu_\alpha | \nu_i \rangle. \tag{2}$$

In case of three neutrino flavors, it's known as the Pontecorvo-Maki-Nakagawa-Sakata mixing matrix, and it transforms the mass eigenstates $(1, 2, 3)$ with mass eigenvalues m_1, m_2, and m_3 to the flavor eigenstates (e, μ, τ) and can be parameterized as

$$U_{\mathrm{PMNS}} = \begin{pmatrix} 1 & 0 & 0 \\ 0 & C_{23} & S_{23} \\ 0 & -S_{23} & C_{23} \end{pmatrix} \begin{pmatrix} C_{13} & 0 & \hat{S}_{13}^* \\ 0 & 1 & 0 \\ -\hat{S}_{13} & 0 & C_{13} \end{pmatrix} \begin{pmatrix} C_{12} & S_{12} & 0 \\ -S_{12} & C_{12} & 0 \\ 0 & 0 & 1 \end{pmatrix} \begin{pmatrix} e^{i\Phi_1} & & \\ & e^{i\Phi_2} & \\ & & 1 \end{pmatrix}, \tag{3}$$

where $C_{jk} = \cos\theta_{jk}$, $S_{jk} = \sin\theta_{jk}$, $\hat{S}_{13} = e^{i\delta_{CP}}\sin\theta_{13}$. Φ_1 and Φ_2 are the so called Majorana phases[1], and as it will be shown later on in this text, these Majorana phases do not contribute to the neutrino oscillations.

2.2 Neutrino oscillations

Taking into account the above mixing of mass eigenstates, the propagation of the flavor eigenstates becomes more interesting. In quantum mechanics the evolution of

---

[1]Because neutrinos have zero electric charge, they can be theoretically Dirac or Majorana particles. Φ_1 and Φ_2 phases are related to the Majorana's theory. This is well described for example in [1].

any state is determined by the well-known Schrödinger equation[1]

$$i\frac{d}{dt}|\psi(t)\rangle = \hat{H}(t)|\psi(t)\rangle, \tag{4}$$

where $\hat{H}$ is a Hamiltonian operator which is in general time-dependent, and $|\psi(t)\rangle$ is an arbitrary state vector. Now, assuming a time-independent Hamiltonian, with no interactions, thus no potential present, the time evolution of the flavor eigenstate α can be written out as

$$|\nu_\alpha(t)\rangle = e^{-i\hat{H}t}|\nu_\alpha(0)\rangle. \tag{5}$$

The probability that the state α will change into state β after time t is defined as

$$p_{\alpha\to\beta}(t) = |\langle\nu_\beta(0)|\nu_\alpha(t)\rangle|^2. \tag{6}$$

To get the amplitude of this process, the "bra" vector $\langle\nu_\beta|$ can be applied on the "ket" vector (5), and one gets

$$\langle\nu_\beta(0)|\nu_\alpha(t)\rangle = \langle\nu_\beta|e^{-i\hat{H}t}|\nu_\alpha\rangle = \langle\nu_\beta|\nu_i\rangle\langle\nu_i|e^{-i\hat{H}t}|\nu_j\rangle\langle\nu_j|\nu_\alpha\rangle =$$
$$= \sum_i U_{\alpha i}^* U_{\beta i} e^{-iE_i t}, \tag{7}$$

where the completeness relation $\sum_i |\nu_i\rangle\langle\nu_i| = I$ (I stands for identity operator) was used along with relation (2) and the fact that $|\nu_i\rangle$ are actually eigenstates of the Hamiltonian with eigenvalues E_i[†]. To simplify the expressions, the notation of time 0 is omitted.

Now, combining (6) and (7) one obtains

$$p_{\alpha\to\beta}(t) = \sum_{ij} U_{\alpha i}^* U_{\beta i} U_{\alpha j} U_{\beta j}^* e^{-i\Delta E_{ij}t} =$$
$$= \sum_{ij} Re\left(U_{\alpha i}^* U_{\beta i} U_{\alpha j} U_{\beta j}^*\right)\cos(\Delta E_{ij}t) +$$
$$+ \sum_{ij} Im\left(U_{\alpha i}^* U_{\beta i} U_{\alpha j} U_{\beta j}^*\right)\sin(\Delta E_{ij}t),$$

and using relations for cosine of double argument, the fact that the matrix U is unitary, and the symmetry (antisymmetry) in ij of real (imaginary) part of $U_{\alpha i}^* U_{\beta i} U_{\alpha j} U_{\beta j}^*$, more convenient form for the probability is

$$p_{\alpha\to\beta}(t) = \delta_{\alpha\beta} - 4\sum_{i>j} Re\left(U_{\alpha i}^* U_{\beta i} U_{\alpha j} U_{\beta j}^*\right)\sin^2(\Delta\frac{E_{ij}}{2}t) +$$
$$+ 2\sum_{i>j} Im\left(U_{\alpha i}^* U_{\beta i} U_{\alpha j} U_{\beta j}^*\right)\sin(\Delta E_{ij}t). \tag{8}$$

ΔE_{ij} is the standard way how to express subtraction of energies $E_i - E_j$.

These oscillations are often called vacuum oscillations, as no interaction was considered in previous calculations. However, matter affects the oscillations and for high densities like in the Sun this effect is indispensable. But in conditions relevant for short-baseline experiments[3], it can be neglected in the first order.

---

[1]Unless stated otherwise, there will be used the natural system of units, in which $\hbar = c = 1$.

[†]Hamiltonian with only mass and kinetic terms is considered, therefore the states with definite mass and definite momentum are stationary.

[3]Details on modifications for the oscillations in matter can be found in [2].

2.2.1   2 flavor case

For demonstration of oscillations it is common to consider simple case of two neutrino species, e.g. ν_e and ν_μ. The mixing matrix U can be written as

$$U = \begin{pmatrix} c & s \\ -s & c \end{pmatrix}, \tag{9}$$

where $c = \cos\theta$, $s = \sin\theta$, and θ is the only parameter of this unitary matrix. Now, one can find, for example, the survival probability of the electron neutrino, which is straightforward using (8):

$$p_{e\to e}(t) = 1 - 4\sin^2\theta\cos^2\theta\sin^2\frac{\Delta E_{12}t}{2} = 1 - \sin^2 2\theta\sin^2\frac{\Delta E_{12}t}{2}. \tag{10}$$

As the neutrinos are known to be very light, the energy can be written in a relativistic approximation even for low energies of the order of MeV. So for $p \gg m$ it could be taken as

$$E = p\sqrt{1 + \frac{m^2}{p^2}} \approx p + \frac{1}{2}\frac{m^2}{p} \approx p + \frac{m^2}{2E} \tag{11}$$

It is also convenient to rewrite the survival probability in terms of the distance L traveled by neutrinos. For relativistic neutrinos $L \approx t$ and one has

$$p_{e\to e}(L) = 1 - \sin^2 2\theta\sin^2\frac{\Delta m_{12}^2 L}{4E}, \tag{12}$$

where $\Delta m_{12}^2 = m_1^2 - m_2^2$. The transition probability, i.e. the probability that muon neutrino can be found instead the initial electron neutrino, after traveling distance L is simply

$$p_{\nu_e\to\nu_\mu}(L) = 1 - p_{\nu_e\to\nu_e}(L) = \sin^2 2\theta\sin^2\frac{\Delta m_{12}^2 L}{4E}. \tag{13}$$

So, while neutrino travels, both probabilities oscillate along the track with wavelength $E/(\pi\Delta m_{12}^2)$ and with the amplitude determined by mixing parameter θ. There would be no oscillation in case that neutrinos were massless or the mixing angle was equal 0. On the other hand, if the mixing is maximal, i.e. $\theta = \pi/4$, then there is a distance where electron neutrino surely disappears.

2.2.2   3 flavor case

The way how to get survival (disappearance) probability in case that there are 3 neutrino species is the same as for 2 neutrinos, but it costs a bit more effort to work it out.

From previous example it is obvious that the probability oscillates only if at least one neutrino is massive. Frequencies of oscillations are proportional to the difference of squared masses and the amplitudes may depend on mixing angles θ_{12}, θ_{13} and θ_{23}, as well as on the additional phase δ_{CP}. But they do not depend on the Majorana phases Φ_1 and Φ_2. Indeed, if one uses the U_{PMNS} matrix form (3) in the amplitude (7), the following expression comes out

$$\langle\nu_\beta|\nu_\alpha(t)\rangle = \sum_i U'_{\beta i}U'^*_{\alpha i}u_i u_i^* e^{-iE_i t}, \tag{14}$$

where the matrix U_{PMNS} was split as $U_{\text{PMNS}} = U' \cdot diag(e^{i\Phi_1}, e^{i\Phi_2}, 1) = U' \cdot diag(u_1, u_2, u_3)$, matrix multiplication of a matrix U', depending on mixing angles and CP-phase, and a diagonal matrix with Majorana phases. It's obvious that $u_i u_i^* = 1^\dagger$, and hence the independence of the oscillations on Majorana phases is now clear.

For the following calculations, the above presented matrix U' will be used, so it would be handy to show it's elements:

$$U' = \begin{pmatrix} C_{12}C_{13} & S_{12}C_{13} & \hat{S}_{13}^* \\ -S_{12}C_{23} - C_{12}S_{23}\hat{S}_{13} & C_{12}C_{23} - S_{12}S_{23}\hat{S}_{13} & S_{23}C_{13} \\ S_{12}C_{23} - C_{12}S_{23}\hat{S}_{13} & -C_{12}C_{23} - S_{12}S_{23}\hat{S}_{13} & S_{23}C_{13} \end{pmatrix}. \tag{15}$$

The notation is the same as in expression (3) in 2.1.

Since in the reactor neutrino experiments the survival probability of electron neutrino is relevant, let's concentrate on the probability $p_{e\to e}$. Again, introducing (15) into (8) one gets

$$p_{e\to e}(t) = 1 - 4\left[S_{12}^2 C_{12}^2 C_{13}^4 \sin^2\frac{\Delta E_{12}t}{2} + C_{12}^2 S_{13}^2 C_{13}^2 \sin^2\frac{\Delta E_{13}t}{2} + S_{12}^2 S_{13}^2 C_{13}^2 \sin^2\frac{\Delta E_{23}t}{2} \right],$$
$$\tag{16}$$

and after a simple manipulation

$$p_{e\to e}(t) = 1 - \sin^2 2\theta_{12} \cos^4\theta_{13} \sin^2\frac{\Delta E_{12}t}{2} - \sin^2 2\theta_{13} \cos^2\theta_{12} \sin^2\frac{\Delta E_{13}t}{2} -$$
$$- \sin^2 2\theta_{13} \sin^2\theta_{12} \sin^2\frac{\Delta E_{23}t}{2}. \tag{17}$$

Similarly to the two-neutrino case, it is more convenient to write the probability in a relativistic approximation and dependent on the traveled distance L

$$p_{e\to e}(L) = 1 - \sin^2 2\theta_{12} \cos^4\theta_{13} \sin^2\left(\frac{\Delta m_{21}^2}{4E}L\right) - \sin^2 2\theta_{13} \cos^2\theta_{12} \sin^2\left(\frac{\Delta m_{31}^2}{4E}L\right) -$$
$$- \sin^2 2\theta_{13} \sin^2\theta_{12} \sin^2\left(\frac{\Delta m_{32}^2}{4E}L\right). \tag{18}$$

2.3 Current knowledge of mixing parameters

Present experiments measuring neutrino oscillations are classified according to their neutrino source, i.e. accelerator, reactor, solar and atmospheric neutrino experiments. There will be no more discussions on the particular classes except a review which processes are they sensitive to and what parameters are they allowed to measure. The reactor experiments themselves are described in more details in the subsection 2.5.

The type oscillation on which experiment can be sensitive is determined by the energy spectrum of measured neutrinos and the distance L of detector from source. According to mixing parameters, measurements may be optimized for exploration of transition or survival probabilities.

The accelerator neutrino experiments (LSND, Karmen, etc.) are sensitive to the $\nu_\mu \to \nu_\tau$ transition with allowed measurement of θ_{23} and Δm_{32}^2. In future they are

---

†No summation convention used.

planned to be sensitive to ν_μ disappearance through $\nu_\mu \to \nu_e$ transition with possible search for θ_{13} and CP violation.

The reactor neutrino experiments (Chooz, KamLAND, Palo Verde etc.) are sensitive to $\bar{\nu}_e$ disappearance measuring θ_{13} and Δm^2_{32} on short (<5 km) distances from source and θ_{12} and Δm^2_{21} on long distances ($\sim$100 km).

Another measurements of θ_{12} and Δm^2_{21} are achieved by solar neutrino experiments (e.g. SNO, Homestake, Super-Kamiokande) for the Sun is prolific source of electron neutrinos. The parameters can be extracted from measurement of ν_e disappearance.

Atmospheric neutrino experiments (Frèjus, IMB, Kamiokande, Super-Kamiokande etc.) measure θ_{23} and Δm^2_{32} from ν_μ disappearance through $\nu_\mu \to \nu_\tau$ transition.

Particle Data Group presents in its Review of Particle Physics [3] the following values of parameters $\theta_{12}, \theta_{13}, \theta_{23}, \Delta m^2_{21}$, and Δm^2_{32}.

$$\sin^2(2\theta_{12}) = 0.86^{+0.03}_{-0.04}$$
$$\Delta m^2_{21} = (8.0 \pm 0.3) \times 10^{-5} \text{eV}^2 \tag{19}$$

These are fits from results of solar neutrino experiments and KamLAND. The sign of the above mass squared difference is defined to be positive.

Next ranges are from results of Super-Kamiokande and correspond to the projections onto the appropriate axes of the 90% CL contours in the Δm^2_{32}–$\sin^2(2\theta_{32})$ plane.

$$\sin^2(2\theta_{23}) > 0.92$$
$$\left|\Delta m^2_{32}\right| = (1.9 \text{ to } 3.0) \times 10^{-3} \text{eV}^2 \tag{20}$$

The sign of Δm^2_{32} is unknown.

The parameter θ_{13} has only an upper limit. This one is from results of experiment CHOOZ for the 90% CL and for $\Delta m^2_{32} = 1.9 \times 10^3 \text{eV}^2$.

$$\sin^2(2\theta_{13}) < 0.19 \tag{21}$$

We can conclude that, unlike θ_{12} and θ_{23}, the mixing angle θ_{13} is very small, may be vanishing. The three parameters that are not determined by present data are θ_{13}, the sign of Δm^2_{32}, and the Dirac CP-violating phase δ_{CP}.

The unknown sign of Δm^2_{32} raises a question about the neutrinos' mass hierarchy. The options that are usually called normal and inverted hierarchy are

$$m_1^2 < m_2^2 < m_3^2 \tag{22}$$
$$m_3^2 < m_1^2 < m_2^2. \tag{23}$$

2.4 Significance of the mixing angle θ_{13}

As one of the six neutrino mixing parameters measurable in neutrino oscillations, θ_{13} is important in its own right and for further studies of neutrino oscillations. In the mixing matrix (15), the angle θ_{13} is closely bounded to the CP-violating phase δ_{CP}. To design experiments to measure the phase there's need of sufficient precision of θ_{13}. The matter effect, which can be used to determine the mass hierarchy, also depends on the size of θ_{13}.

If $\theta_{13} > 0.01$, then the design of future experiments searching for CP violation seems to be relatively straightforward [4]. However, for smaller θ_{13} new experimental techniques and accelerator technologies are likely to be required to carry out the measurements. In addition, θ_{13} is important in theoretical model building of the neutrino mass matrix, which can serve as a guide to the theoretical understanding of physics beyond the standard model.

The February 28, 2006 report of the Neutrino Scientific Assessment Group (NuSAG) [5], which advises the US DOE[1] Offices of Nuclear Physics and High Energy Physics and the National Science Foundation, recommends with high priority a reactor anti-neutrino experiment to measure $\sin^2 2\theta_{13}$ at the level of 0.01.
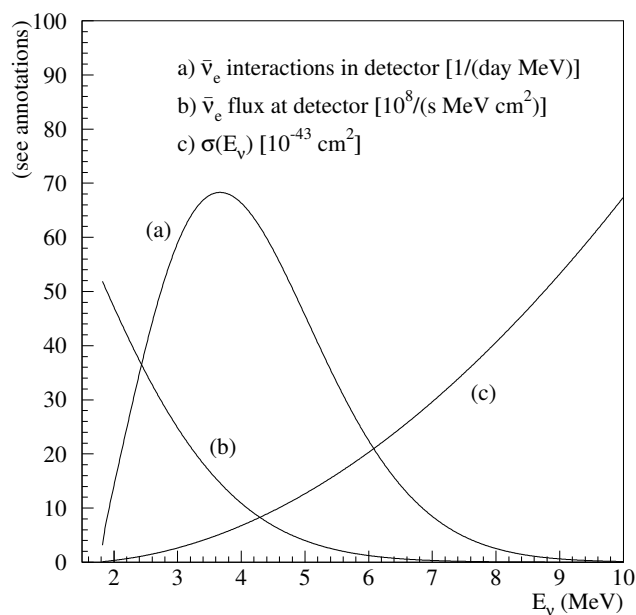
Figure 1: Reactor $\bar{\nu}_e$ flux, inverse beta decay cross section, and $\bar{\nu}_e$ interaction spectrum at a detector based on such reaction. The figure is taken from [7].

2.5 Determining θ_{13} with nuclear reactors

Nuclear reactors are relatively prolific sources of neutrinos as approximately 6 neutrinos are produced on average by each fission process. Fission reactions in reactor produce daughter particles many of which beta decay producing $\bar{\nu}_e$, because they are rich in neutrons. There are four main fission components, ^{235}U, ^{238}U, ^{239}Pu, and ^{241}Pu, each having a different energy spectrum for neutrinos, and fraction of each in the fuel is developing in time. As a consequence, the energy spectrum of neutrinos in a flux from reactor is time dependent as well[2]. The expected count rate in the detector, considering no oscillations, is proportional to the product of differential energy distribution in a flux of neutrinos and the total cross section of inverse beta decay.

---

[1]American Department of Energy

[2]More on this topic can be found in [6].

These are plotted in fig. 1 as well as the expected count rate. The highest rate of interactions occurs at $E_\nu \approx 4$ MeV.

Now, let's have a look at electron anti-neutrino survival probability. Because θ_{13} is so small[1], the equation (18) can be written in the following form:[2,3]

$$p_{\bar{\nu}_e \to \bar{\nu}_e} = 1 - P_{12} - P_{13}, \tag{24}$$

where the term

$$P_{12} = \sin^2 2\theta_{12} \cos^4 \theta_{13} \sin^2 \left(\frac{\Delta m_{21}^2}{4E} L \right) \approx \sin^2 2\theta_{12} \sin^2 \left(\frac{\Delta m_{21}^2}{4E} L \right) \tag{25}$$

is insensitive to θ_{13} in contrast to the term

$$P_{13} = \sin^2 2\theta_{13} \cos^2 \theta_{12} \sin^2 \left(\frac{\Delta m_{31}^2}{4E} L \right) - \sin^2 2\theta_{13} \sin^2 \theta_{12} \sin^2 \left(\frac{\Delta m_{32}^2}{4E} L \right) \approx$$

$$\approx \sin^2 2\theta_{13} \sin^2 \left(\frac{\Delta m_{32}^2}{4E} L \right), \tag{26}$$

where the fact that $\Delta m_{31}^2 \approx \Delta m_{32}^2$ has been considered. Thus, for the survival probability, one obtains

$$p_{\bar{\nu}_e \to \bar{\nu}_e} \approx 1 - \sin^2 2\theta_{12} \sin^2 \left(\frac{\Delta m_{21}^2}{4E} L \right) - \sin^2 2\theta_{13} \sin^2 \left(\frac{\Delta m_{32}^2}{4E} L \right). \tag{27}$$

This relation is plotted in fig. 2 along with terms P_{12} and P_{13}. On the figure, the first maximum of the term sensitive to θ_{13} is somewhere around 2 and 3 km and there this term is dominating. Taking this into account, it is desirable to build detector at a distance of a few kilometers from the reactor.[4]

---

[1]Or may be vanishing at all, see upper limit (21) in section 2.3.

[2]To use the same relation for neutrinos and anti-neutrinos, the CPT invariance was assumed.

[3]The probability is now noted as $p_{\bar{\nu}_e \to \bar{\nu}_e}$, unlike the previous expressions, to emphasize that it is the anti-neutrino survival probability.

[4]Note that the engaged probability is for neutrinos with fixed energy. Integrating this probability with energy differential distribution of detected neutrinos, the dependency changes slightly. Also the value of Δm_{32}^2 used in the figure is lower limit for the parameter. Varying it causes shifting of the maximum.
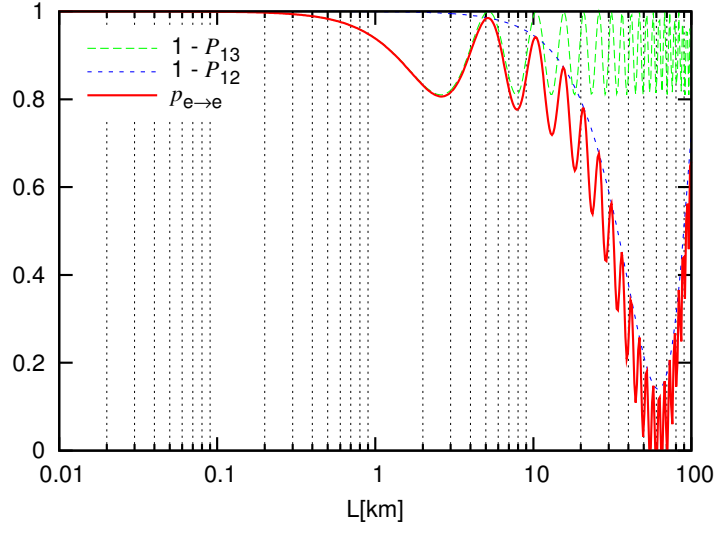
Figure 2: Survival probability of electron neutrino with energy $E = 4$ MeV as expressed in eq. (27)—red line. Contributions from individual terms are also plotted, separately. The parameters used are $\Delta m_{31}^2 = 1.9 \times 10^{-3} \text{eV}^2$, $\Delta m_{21}^2 = 8 \times 10^{-5} \text{eV}^2$, $\sin^2(2\theta_{13}) = 0.19$, and $\sin^2(2\theta_{12}) = 0.86$.

3   Experiment Daya Bay

The goal of the Daya Bay reactor anti-neutrino experiment is to determine the unknown neutrino mixing angle θ_{13} with a sensitivity of 0.01 or better in $\sin^2 2\theta_{13}$, an order of magnitude better than the current limit (21).

The experiment is now in stage of research and development[1]. The preliminary design is described in the Conceptual design report (CDR), [6]. The following brief description is extracted from the report.

3.1 $\bar{\nu}_e$ detection

The first experiment which detected neutrinos was made by F.Reines and C.Cowan in 1956. The principle of detection consisted in using a target made of around 400 liters of water. When the anti-neutrino coming from the nuclear reactor went through the target, it interacted with a proton, giving a positron and a neutron. This gave the possibility to trigger on two signals. First from the positron annihilation, the second from the neutron capture. See a sketch in fig. 3.
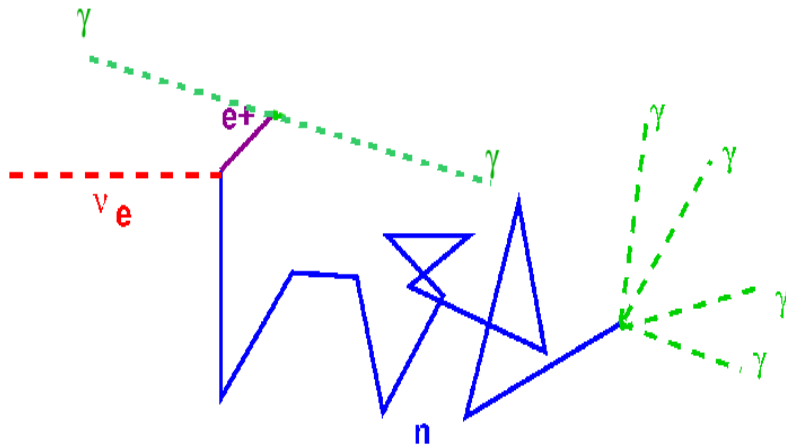
Figure 3: A sketch of $\bar{\nu}_e$ interaction with proton in water, producing neutron and positron signal.

Generaly, in a weak interaction of $\bar{\nu}_e$ with a proton, the emerged positron slows down and stops quickly in matter and then it annihilates with surrounding electron producing two gammas with total energy 1022 keV. This makes a first signal, the so-called prompt signal, which raised from the ionization loss and the subsequent annihilation. The energy associated with this signal is termed the prompt energy, E_p.

The prompt energy is related to the neutrino energy through the relation

$$E_e \simeq E_\nu - (M_n - M_p), \tag{28}$$

where E_e is the positron energy, E_ν is the energy of the anti-neutrino, and $M_n - M_p$ is the difference between neutron and proton masses. This relation is only zeroth order

---

[1]Civil construction started in June this year.

approximation in $1/M$—inverse nucleon mass—where the neutron recoil energy was neglected.

The second particle from neutrino interaction, neutron, is thermalized during its first 10 μs of existence in the detector. After that interval, neutron captures with probability depending on time according to the exponential law

$$P_n = \frac{1}{\tau}e^{-\frac{t}{\tau}}, \tag{29}$$

where P_n is the probability, that neutron is still not captured after time t elapsed from thermalization. τ is the mean life time. After the capture, a resulting nucleus de-excites producing gamma cascade. The total energy released varies with target nucleus and gives delayed signal.

In the water, the mean life time of a neutron is about 200 μs, [8], and the total energy released is 2.2 MeV. This opens large time window between prompt and delayed signal to gather small amount of energy. The accidental background may produce signal with total energy which can mimic the neutron signal. The probability of such fake signal increases with the time window in which the delayed signal can arrive. This yields in high background rate. Therefore, some additional doping is needed to provide isotopes with large cross section for the capture of thermal neutrons and with higher energy release.

The group of Reines and Cowan improved the way of detection, and presented liquid scintillator with cadmium dopant as a possible solution. In the article [9], they proposed several variations of liquid scintillators appropriate for use.

In case of Daya Bay experiment, the detector contains liquid scintillator doped with gadolinium. More on this design can be found in the following subsections.

3.2 Experimental layout

The experimental site takes place by the Daya Bay nuclear power complex, about 55 km north-east from Victoria Harbor in Hong Kong, southern China (see the map in fig. 4). The complex consists of three nuclear power plants (NPPs): the Daya Bay NPP, the Ling Ao NPP, and the Ling Ao II NPP. The Ling Ao II NPP is under construction and will be operational by 2010–2011. Each plant has two identical reactor cores, and each core generates 2.9 GW of thermal energy during normal operation. The Ling Ao cores are about 1.1 km east of the Daya Bay cores, and about 400 m west of the Ling Ao II cores.

The experiment design consists of three underground halls with detectors. Two are located by the Daya Bay and Ling Ao NPPs and are called the Daya Bay near site and Ling Ao near site, respectively. The third hall is placed around 2 km from the reactors, in location with strong overburden of about 900 meters of water equivalent. The schematic view of the location is in fig. 5.

3.3 Detector design

The detector consists of multiple cylindrical anti-neutrino detector modules submerged into water pool, which makes shielding against radiation from the surrounding rock and minimizes background due to muon spallation products. The water pool is

Figure 4: Daya Bay and vicinity: The nuclear power complex is located about 55 km from central Hong Kong. The map is taken from [10].

Figure 5: Schematic plan of experimental site. The Daya Bay near detector site is located 363 m from the center of the Daya Bay cores with overburden 98 m of rock (255 m.w.e.). The Ling Ao near detector hall is 481 m from the center of the Ling Ao cores, and 526 m from the center of the Ling Ao II cores where the overburden is 112 m (291 m.w.e). The distances from the far detector to the Daya Bay and to the Ling Ao–Ling Ao II cores are 1985 m and 1615 m, respectively. The overburden is about 350 m (910 m.w.e).

also used as a Cherenkov detector tagging through going cosmic muons. Both near sites are planned to have two modules each, and there will be four of them in the far

hall.

The water pool is covered with RPC[1] modules which are employed as additional muon tracker. These modules together with the water shielding present the whole muon detector system.
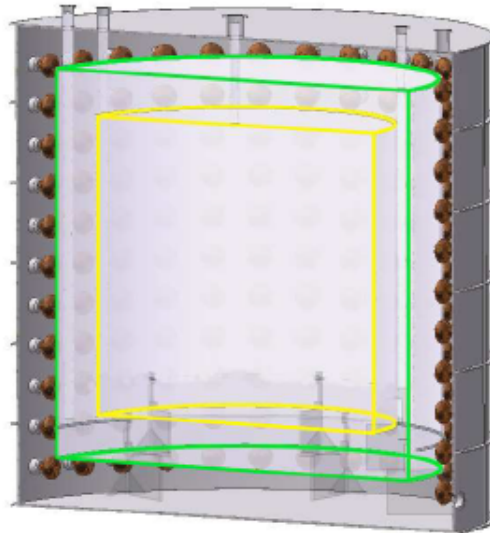

Figure 6: Cross section of three-zone anti-neutrino detector module showing two acrylic vessels and PMTs mounted on the inside walls of the stainless steel tank. Picture taken from [10].

3.4   Anti-neutrino detector module

The module is constructed in form of three nested cylindrical zones partitioned with acrylic tanks and bounded by stainless steel tank. The innermost tank is filled with gadolinium-loaded organic liquid scintillator, Gd-LS, serving as an anti-neutrino target. The middle layer is filled with pure liquid scintillator and is called "gamma catcher", for it is employed to catch all gammas escaping from target volume. The scintillation light coming from both volumes is detected by photomultiplier tubes (PMTs) mounted on the inner side of the steel tank. The gamma catcher is embedded in a mineral oil buffer, which provides shielding against gamma radiation from the PMTs mainly and also from the steel tank. The sizes of the volumes are 20 tons for each liquid scintillator and 40 tons for mineral oil. On fig. 6, there is a cross section through the proposed module, and its dimensions are summarized in table 1.

3.5   Muon detector

The muon detector is designed for a purpose of muon tagging with high efficiency, which is required to be better than 99.5%. To achieve such efficiency, three detector systems are employed, inner and outer water shields, and a muon tracker made out of four layers of RPC modules. The muon system is not envisioned to act as an on-

---

[1]RPC is an abbreviation of resistive-plate chamber.

Region	IR[m]	OR[m]	inner height[m]	outer height[m]	thickness[mm]	material
target	0.00	1.60	0.00	3.20	10.0	Gd-LS
γ-catcher	1.60	2.05	3.20	4.10	15.0	LS
oil buffer	2.05	2.50	4.10	5.00	8.0-10.0	Mineral oil

Table 1: Dimensions of the mechanical structure and materials of the anti-neutrino detector module. IR and OR denote inner and outer radius, respectively, LS and Gd-LS are pure organic and Gadolinium doped liquid scintillators.

line veto. It will provide extensive measurement of through passing muons instead, allowing careful offline studies to optimize the performance of the system.

The pool, in which the anti-neutrino detector modules are immersed, has a rectangular shape in the case of near halls and a square shape in the case of far hall. The modules are placed 1 m from each other, and their minimum distance from walls of the pool is 2.5 m. The overall dimensions are 16m × 10m × 10m(height) and 16m × 16m × 10m(height) for near halls and far halls respectively.

The water shield is divided into inner and outer section and instrumented with photo-tubes to detect Cherenkov photons from muons impinging on the water. The outer side and bottom sections of the pool are 1 m thick and read out by photo-tubes spaced periodically and facing in both directions, inward and outward. The sections are separated by Tyvek film reflectors stretched over a stainless steel frame. The frame holds PMTs for both the inner and outer sections of the pool. The PMTs are approximately evenly distributed forming a rectangular grid with a densities of 1 PMT per 4 m^2 for the inner and 1 PMT per 6–7 m^2 for the outer water shield. This corresponds to a ∼0.8% and ∼0.5% areal coverage, respectively.

The muon tracker is completed by four layers of resistive plate chambers above the pool which extend 1 m beyond the edge of the pool in all directions, both to minimize the gaps in coverage and to allow studies of background caused by muon interactions in the rocks surrounding the pool. The simplified cross-sectional diagram of the pool with submerged detector modules is on the image in fig. 7.

3.6 Systematic uncertainties

Since the experiment's demand on the sensitivity is so high, the control of systematic uncertainties is critical. There are three main sources of systematic uncertainties: reactor, background, and detector. In order to achieve the $\sin^2(2\theta_{13})$ sensitivity below 0.01 at 90% confidence level, requirements on statistical and systematic uncertainties listed in table 2 need to be granted. Here follows brief description of reactor and detector related uncertainties, and in following subsection more information on backgrounds is presented. For further reference on this topic see the experiment's proposal [10].

Reactor related systematic uncertainties are mainly due to power fluctuations which lead to uncertainty in a neutrino flux. This can be handled by using the near site and far site arrangement. In a simple case where only one core is in use, and anti-neutrinos are detected by detectors at near and far site, all uncertainties related to its flux can be canceled by measuring a relative signal. However, in the
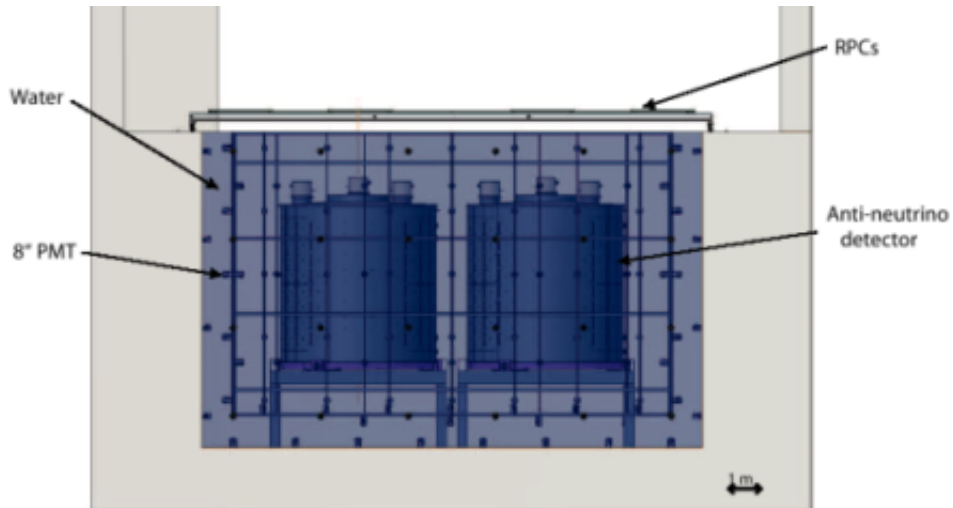
Figure 7: Scheme of muon system. The pool is divided into inner and outer Cherenkov detector and covered with support structure for RPC modules. Taken from [6].

Requirement	Near Site	Far Site
Statistical uncertainty	0.05%	0.16%
Detector systematic uncertainty	0.38%/module	
Reactor power systematic	0.13%	
Background uncertainty	0.3%	0.2%

Table 2: Requirements on uncertainties necessary for achieving the sensitivity goal of $\sin^2(2\theta_{13}) < 0.01$ at 90% confidence level.

Daya Bay NPP case, where multiple reactors are employed, the situation becomes more complicated. Although one must rely on the measured reactor power levels, the triple site arrangement provides a tool to suppress the systematic uncertainty to the required level, even with uncertainty in relative detector–core distances.

Detector related uncertainties are caused by several factors. As the anti-neutrino targets are free protons in the detector, the event rate is proportional to their total mass. The systematic uncertainty in knowledge of the number of free protons relies upon exact knowledge of the target volume, as well as on the knowledge of the hydrogen to carbon ratio of the liquid scintillator. This implicates the necessity to take a special care of the filling of the module with accurate measurement of liquid flow. There are methods and instruments for precise measurement of H/C ratio which are suitable for the case of the Daya Bay experiment, e.g. Coriolis mass flow meters.

For anti-neutrino detecting, delayed coincidence is used for prompt positron and delayed neutron signal. The positron visible energy has threshold of 1.022 MeV. Due to finite detector energy resolution of ∼12% at 1 MeV the reconstructed energy will have a tail below 1 MeV. Therefore positron detection efficiency using the 1 MeV energy cut brings another uncertainty. This effect has been studied by MC simulations resulting in estimated uncertainty 0.05%. Contribution of the upper energy limit 8 MeV for the positron signal is negligible.

Similar uncertainty arises from the neutron detection efficiency, since the neutrons

that capture on Gd are detected, yielding at least 6 MeV of visible energy from the resulting capture γ rays, during the time period $0.3 < T < 200$ μs after the prompt signal. The efficiency ϵ_n for detecting the neutron is then given by

$$\epsilon_n = P_{Gd}\epsilon_E\epsilon_T \tag{30}$$

in which P_Gd is the probability of capture on gadolinium[1], ϵ_E is the efficiency of the $E > 6$ MeV energy cut for Gd capture, and T is the efficiency of the delayed time period cut. Each term contributes to the total uncertainty in ϵ_n which is assumed to be less than 0.25%.

Other contributors are neutron multiplicity cut and trigger efficiencies which are to be known to uncertainty better than 0.05%.

In order to further reduce all detector related uncertainties, system of tunnels connecting all sites will be exploited for near-to-far site detectors swapping. It's planned to have each detector taking data half time at near site and half time at far site.

Moreover, the feature of multiple detectors at each site allows a cross-calibration, which is important for further studies of detector response.

3.7 Backgrounds

In reactor neutrino experiments, it is usual to detect tens to hundreds of anti-neutrinos per day, depending on the flux at the detector site and the target volume. Such a low signal rate requires a special treatment of backgrounds in order to get a reasonable signal to noise ratio.

Since a detection of $\bar{\nu}_e$ is based on a two signal coincidence trigger, background may be classified as correlated or accidental. The correlated background causes a fake prompt signal, the positron-like signal, and a delayed neutron-like signal, both originating in the same source. The accidental, or uncorrelated, background is caused by two uncorrelated signals, neutron-like after positron-like, accidentally occurring in a specific time window. The rate of such background, R_{acc}, can be expressed as

$$R_{acc} = R_pR_d\tau_d, \tag{31}$$

where R_p and R_d are background rates for the prompt and the delayed events, respectively, and τ_d is the time window. Therefore, in order to reduce accidental events, it is desirable, along with a reduction of the two individual signal rates, to use an appropriate time window cut.

There are three main sources of background: natural radioactivity, cosmic muons, and cosmogenic isotopes.

Natural radioactivity

Naturally occurring radioactivity can create accidental as well as correlated backgrounds. Selection of high purity materials for detector construction and passive shielding provides an efficient protection against this type of background. Also in

---

[1]The concurrent capture is on hydrogen.

order to prevent accumulation of radon in the air, some air purification technique may be employed.

Gamma, beta, and neutron sources may generate accidental events which mimic prompt signal. Delayed signal is mainly caused by neutron capture on Gd. The goal is to reduce the rate of these accidental signals below 50Hz.

Cosmic muons

Cosmic muons are main source of background. They produce neutrons in spallation reactions with matter. Those neutrons may have high energies and can travel through the detector producing tertiary particles, including protons and neutrons giving signals in the detector. Such events may have very complex time structure and can mimic prompt and delayed signal. The energetic spallation neutrons are called fast neutrons.

Some muons may stop in the detector or its surrounding, and, in case of μ^-, they can be captured by nucleus which consequently decays often producing one or more neutrons. The muon capture will be discussed later.

In order to lower the rate of cosmic muons, it servers as a convenient practice to place a detector into underground hall with sufficient overburden. In addition, to overrule remaining cosmic muons, a veto system may be engaged which can tag passing muons.

Table 3 presentes a muon flux for different sites. The number of passing muons at far site is well suppressed by the overburden of the mountain.

	DYB site	LA site	Mid site	Far site
Vertical overburden (m)	98	112	208	355
Muon Flux (Hz/m^2)	1.16	0.73	0.17	0.04
Muon Mean Energy (GeV)	55	60	97	138

Table 3: Muon flux at both near sites (Daya Bay—DYB,Ling Ao—LA), middle site (Mid), and far site, along with corresponding overburden and mean energy.

Cosmogenic Isotopes

The third main source is correlated to the cosmic muons, too. These are so called cosmogenic isotopes. They are produced by muons interacting with matter and are unstable decaying with emission of neutrons. The most significant are ^{8}He and ^{9}Li, because they have a long life time, and thus the produced neutron is difficult to assign to its parent muon. Such isotopes seem to be mostly produced in showers caused by muons[1], thus a longer veto may be applied when showering muon appears.

3.7.1 Stopping muons

Since muon's mean life time is about $\tau_\mu \sim 2.2$ μs ($c\tau_\mu \doteq 659$ m, [3]), only stopped muons decay in the location of the detector, producing electron or positron and

---

[1]KamLAND found that most ^{8}He/^{9}Li background are produced by showering muons and that roughly 3% of cosmic muons shower in a detector, [11].

two relevant neutrinos. The process of slowing down and stopping is estimated to be relatively negligible ($\sim 10^{-10}$ s), compared to the muon's life time. However, negatively charged muon mostly forms muonic atom with a surrounding element, and after that, it can either decay or be captured by the atomic nucleus, usually resulting in production of a neutron and a neutrino.

The following brief description of the process of muon capture draws from the review [12] by N.C. Mukhopadhyay.

Atomic capture: Once muon reaches a state of no kinetic energy, it is trapped by a host atom in a high momentum state. Since all lower-lying states are unoccupied, muon cascades down rapidly to the lowest quantum state (1S). This de-excitation is through Auger and radiative transitions. For a given atomic number Z, Auger process dominate for higher-lying states, and $(n_1, l_1) \rightarrow (n_2 = n_1 - 1, l_2 = l_1 - 1)$ transitions are preferred, where n_1, l_1 and n_2, l_2 are quantum numbers of the initial and final state, respectively. The probability of radiative transitions is proportional to the cube of energy difference between (n_1, l_1) and (n_2, l_2) orbits and the fourth power of Z. Thus, for light elements, Auger effects dominate down to $n_1 \sim 3$, while, for a heavy element like Ag, radiative transitions take over at $n_1 \sim 6$.

Again, the time taken for the muon to enter the lowest orbit from the instant of its atomic capture is very short, about $\sim 10^{-14}$ s.

Nuclear capture: Now, in its base state, muon can either decay with a rate Λ_d or be captured by nucleus with a rate Λ_c. The ratio of the rates varies for different elements. While, in hydrogen, the capture to decay probability ratio is of the order of 4×10^{-4}, in nuclei around $Z = 11$ it is approximately half to half, and in heavy nuclei ($Z \sim 50$) the ratio is about 25.

For a free muon, the decay rate is given as $\Lambda_d^{\text{free}} = 1/\tau_\mu$, however, since the muon is bound in atomic orbit, the decay rate changes to $\Lambda_d^{\text{bound}} = Q\Lambda_d^{\text{free}}$. Mukhopadhyay assumed [12] that $\Lambda_d^{\text{free}} \propto m_\mu^5$, and that bounded muon has effectively lower mass yielding in $\Lambda_d^{\text{bound}} \propto (m_\mu - \epsilon_\mu)^5$ where ϵ_μ is the muon bounding energy. Therefore, the factor Q can be expressed as

$$Q \cong 1 - 2.5(Z\alpha)^2, \tag{32}$$

with α being the fine structure constant.

As far as the capture is concerned, Goulard and Primakoff [25] made calculations for the total muon capture rate, and interested reader is referred to the publication for more details. For now, it is important that the rate is proportional to the fourth power of Z. Thus, the muon capture takes dominance for heavier elements.

3.8 Sensitivity

To obtain maximum sensitivity, two effects of oscillation will be exploited in the final analysis. If the θ_{13} is non-zero, the total rate deficit due to oscillation will be observable at the far detector. In addition, since neutrinos of different energies oscillate at different frequencies, the energy spectra will differ at near and far site, making thus the spectral distortion measurable.

The measured data will be compared with expected number of events without oscillation. To exclude the assumption of "no oscillation" at 90% confidence level, a global χ^2 analysis will be employed.

The full data taking, i.e. with two near sites and one far site operable, is planned to begin in the middle of the year 2010. However, the first completed experimental hall, the Daya Bay near hall, can be used for detector commissioning. Furthermore, it is possible to conduct a fast experiment using only two detector sites, the near and middle hall, while the rest of tunnels is to be excavated.

In fig. 8 there's plotted the expected sensitivity in the Δm^2_{31}—$\sin^2(2\theta_{13})$ plane after three years data taking along with the reachable sensitivity of the "fast option". For comparison, the current upper limit measured by the Chooz experiment is also plotted. The fig. 9 illustrates the time evolution of the sensitivity.
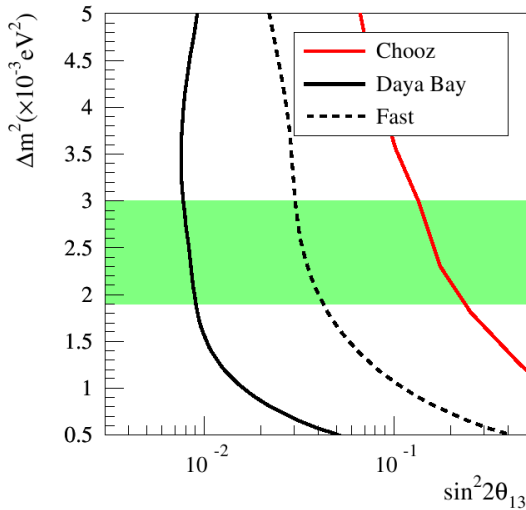

Figure 8: Expected $\sin^2(2\theta_{13})$ sensitivity at 90% C.L. with 3 years of data taking— the solid black line. The dashed line shows the sensitivity of the possible fast measurement with the DYB near site and mid site only. The red line shows the current upper limit measured by Chooz. Picture taken from the proposal [10].
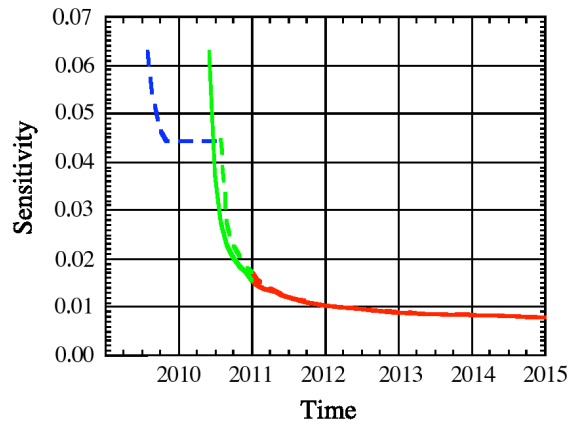

Figure 9: Expected $\sin^2(2\theta_{13})$ sensitivity at 90% C.L. versus time. The solid curve is with two near sites and one far site. The dashed curve includes running first with one near and one mid site. The value of Δm^2_{31} is taken to be 2.5×10^{-3} eV^2. Taken from [6].

4 Muon capture induced neutron background

This work is aimed to give some estimations on how much background could be induced by neutrons from captured μ^-. For this purpose, Monte Carlo simulations were performed using G4dyb software package, which is developed by the Daya Bay collaboration members. The package was used with Geant4.8.2, for main simulations. Monte Carlo methods and software toolkits used in simulations are described in the appendix A.

Another study has been done by Haoqi Lu [13] from the Daya Bay experiment collaboration who had simulated all muons which finally captured in the water pool and looked at how many neutron-like signals and fast neutron signals are detected in anti-neutrino detectors. This work is more concentrated on muons, which are hardly detected by the Cherenkov detector, that means they produce too few Cherenkov photons.

4.1 Cherenkov photon production limit on muons

For muon tagging, the number of fired PMTs threshold, N_{PMT}, is used in the experiment. This means, that the muon-like event has to produce signal in at least N_{PMT} tubes of the water shield in a given time interval τ_μ to be recognized as muon. Such a threshold is due to PMTs' singles rate[1], which is caused mainly by radiation and a dark current. A requirement on dead time τ_{acc} due to accidental coincidence then determines N_{PMT} for the known singles rate R_{singl}. In the Daya Bay experiment the singles rate was assumed to be less than 50 kHz per PMT, and τ_{acc} should be less than 1%. With the experiment's baseline for PMT deployment, the N_{PMT} threshold was determined to be 12.

The probability, that one photon produced by a muon will give a signal in any PMT can be roughly taken as follows

$$P_{\text{signal}} = R_{\text{cov}} \cdot \eta, \tag{33}$$

where R_{cov} is the relative PMT coverage in the water shield, and η is the PMT's quantum efficiency[2], this relation does not include reflection on the walls of the pool. Having peak value[3] of efficiency used in simulations $\eta = 0.15$ and relative coverage of the inner water shield $R_{\text{cov}} = 0.8\%$, the approximate probability is $P_{\text{signal}} = 0.0012$.

Now, one can estimate the number of photons needed to produce signal in N_{PMT} photo-tubes to be $N_{\text{min}} \approx N_{\text{PMT}}/P_{\text{signal}} = 10^4$ photons.

Previous simulations [6] of water shield showed that the number of collected photoelectrons (p.e.) was, in average, more than 7 times greater than expected, which was assumed to be due to the reflections. Knowing this, the probability in (33) may be increased by the factor 7, and the estimation of the limiting number of photons is reduced to $N_{\text{min}} \approx 1.4 \times 10^3$ photons.

---

[1] The mean number of accidental signals per second per PMT.

[2] The meaning of quantum efficiency is described in the appendix C. In (33) should stay collection efficiency along with the quantum one, however, it is convenient to suppose the number η covers both.

[3] The quantum efficiency of photo-tubes varies with wave length of incident photon and is peaked around 400 nm, depending on particular PMT type.

Based on these calculations, muons are considered invisible for the water Cherenkov detector when they produce less than $N_{\text{max}} = 10^3$ Cherenkov photons.

4.2 Generation of muons

The far site hall was chosen for the simulation of capturing muons. The muon flux there is about twenty times smaller than at near sites.

The essential ingredients for muon generator are data obtained from other simulation, where the MUSIC[1] package was used. Muons were transported from the surface to the underground, exploiting precise knowledge of the relief of the mountain coast. For determination of energy and angular distribution on the surface, modified Gaisser formula was employed [10].

A muon generator from G4dyb package uses data file from MUSIC, containing 100 thousand muons, to produce muons with appropriate distribution. The data file doesn't distinguish between negatively and positively charged particles. Hence, when the generator picks out a muon from available data, it determines its sign randomly according to a particular distribution of μ^+/μ^- ratio shown in fig. 10. Since this distribution is limited to 200 MeV/c–120 GeV/c range of muon momentum, the extrapolated ratio is used outside the range, which is 1.4 in original code of the generator for both, the low energy and high energy muons. However, this is evidently wrong looking at the detail in fig. 10 where the ratio tends to be ~1.1 around zero momentum. Having this fixed, more appropriate value 1.1 was used for low energies.
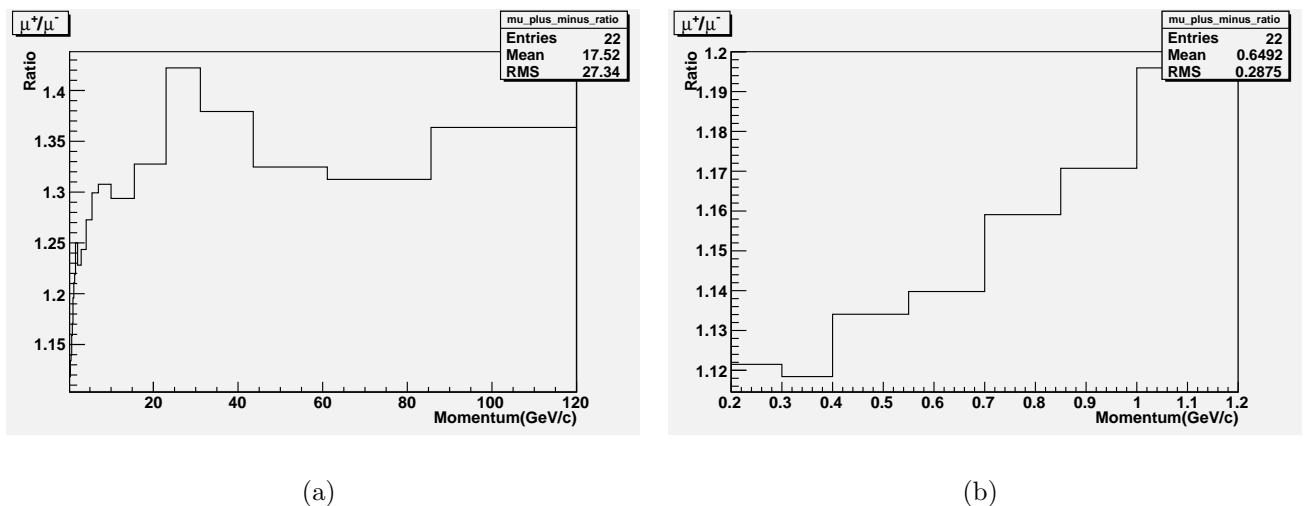

(a) (b)

Figure 10: This is μ^+/μ^- ratio, used by muon generator to decide, whether the output is μ^+ or μ^-. It is limited by range from 200 MeV to 120 GeV. For muons outside the region extrapolated values are used. In(b), there is a detail for momenta from 200 MeV/c to 1200 MeV/c.

In fig. 11, energy distribution of μ^- from the data file is plotted, weighted by the ratio distribution mentioned above. In low energy region, the data underestimate the

---

[1]MUSIC—MUon SImulation Code—is a Monte-Carlo simulation code for muon propagation through the rock [14]. The simulation had been performed by Daya Bay collaborators.

muon flux. Since low energetic muons are crucial for the simulation, the spectrum was shifted by subtracting 150 MeV from the kinetic energy. This could be interpreted as an additional layer of rock, roughly 30 cm. Details are plotted in fig. 11(b).

Muon tracks were initiated from the top and side surfaces of the water pool. The particular surface is randomly chosen with probability proportional to the surface area projected to the plane perpendicular to the muon direction—the size of area as it is seen by the incident muon. The final positions are then uniformly distributed on that surface.
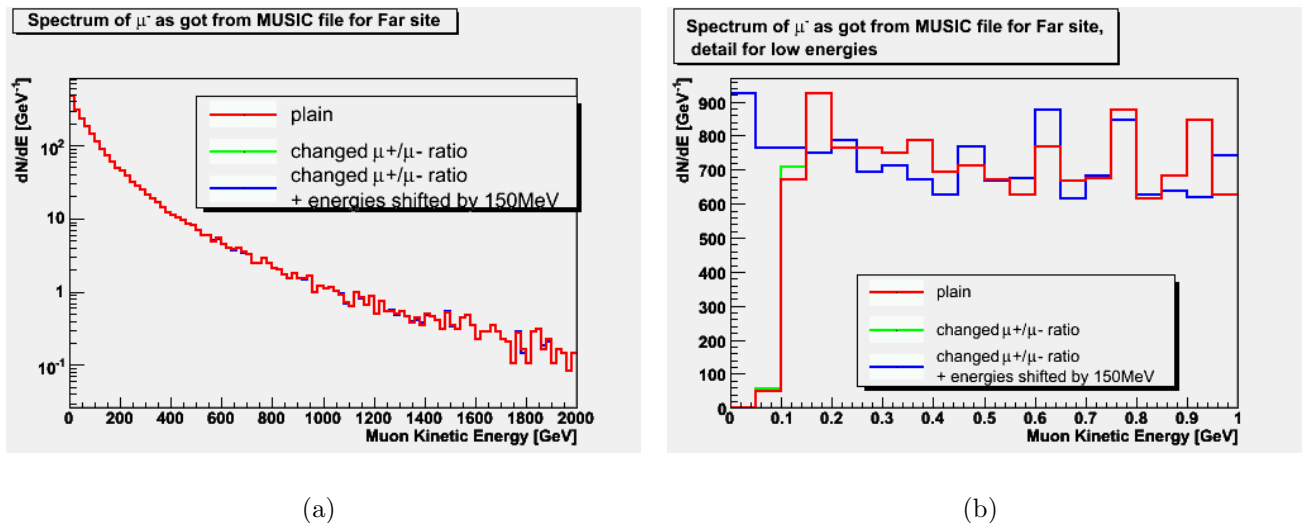

(a)   (b)

Figure 11: Energy distribution of negatively charged muons as got from the generator's data file. Data before and after changes compared: (a) range from 0 up to 2 TeV and (b) is a detail to 1GeV.

4.3   Muon simulation

As discussed above, the muons of interest are those which produce less than 10^3 Cherenkov photons. Preliminary simulations of muons in water pool showed that upper limit on the muon kinetic energy can be used without affecting the number of "invisible muons". See fig. 12 where the dependency of Cherenkov photon number on the initial muon kinetic energy is plotted. The upper limit of 300 MeV was applied on muon generator. Such a cut off decreased significantly a computational time of the simulations.

Other limitations were used in order to speed up the calculations. When the muon became "visible" or it left the area of the water pool, its tracking was stopped, and the event was thrown away.

After the μ^- stops, it can either decay or it can be captured by the nucleus. In appendix A.1, the way how Geant4 treats these processes is described. At the end of μ^-'s track the stop position coordinates, target Z and A, and capture flag[1] were recorded to an output data file.

---

[1]Whether the muon was captured with consequent emission of neutron, or not.

Overall, approximately 7.8 million μ^- with energies under the cut was simulated. It corresponds to 3.3 billion of all muons at far site. In the table 4, concrete numbers are presented along with relative numbers of captures on some elements. A dominant capture is on oxygen.

	# of muons	element	cap./all cap.
generated	7792715	carbon	2.2%
stopped	3736959	oxygen	97.2%
captured	458320	others	0.6%

Table 4: Overall summary of the muon simulation. In the second column there are numbers of muons generated under the limit of 300 MeV, stopped inside water pool generating less than 1000 Cherenkov photons, and—finally—captured producing at least one neutron. Relative numbers of capture on particular elements are presented in the last column.
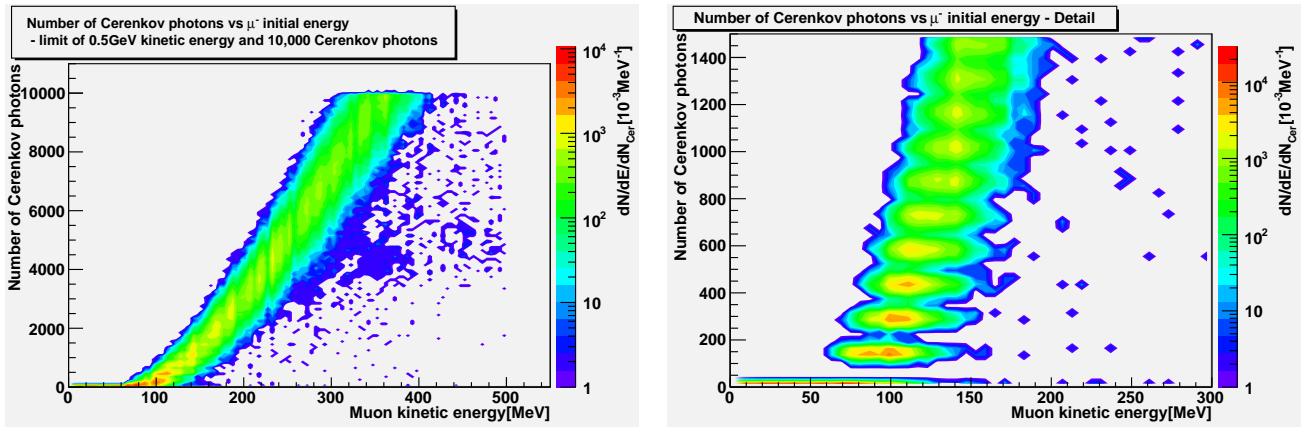
(a)

(b)

Figure 12: Number of produced Cherenkov photons vs. initial kinetic energy of μ^-. (b) Detail. There are visible bunches for low photo emission. This is caused by a use of too long steps in tracking of muons during simulation.

4.4 Neutron generation

Neutron tracks were initiated from positions where muons were stopped and for which the capture flag was set to be true. There have been several problems with Geant4 capture process resulting in wrong neutron spectrum. This is described in the appendix A.1, along with a solution consisting in a use of proper spectra. Therefore, neutrons were given energies according to optional energy distributions. Depending on which element the capture was initiated, the spectra plotted in fig. 13 are used, i.e. for dominating capture on oxygen the corresponding spectrum from fig. 13(b) while for other poorly represented elements the carbon spectrum (fig. 13(a)) was employed.

Again, the preliminary simulation of neutrons had been performed, and plots in fig. 15 show resulting correlation between neutron initial kinetic energy and two distances. The distance from vertex to stop position and the distance from stop position to the nearest surface of GdLS volume. In fig. 15(b) it's evident that neutrons have merely evanescent chance to reach a detector. To achieve higher effectivity of simulation, neutrons were generated only from an interval 30–60 MeV. The lower limit results from previous idea while the upper one is determined by the provided distribution. The number of neutrons taken into account is therefore reduced by a factor ≈13[†].

As far as the angular distribution is concerned, neutrons were generated in an isotropic manner. Furthermore, in order to increase statistics 13 neutrons were generated from each vertex.
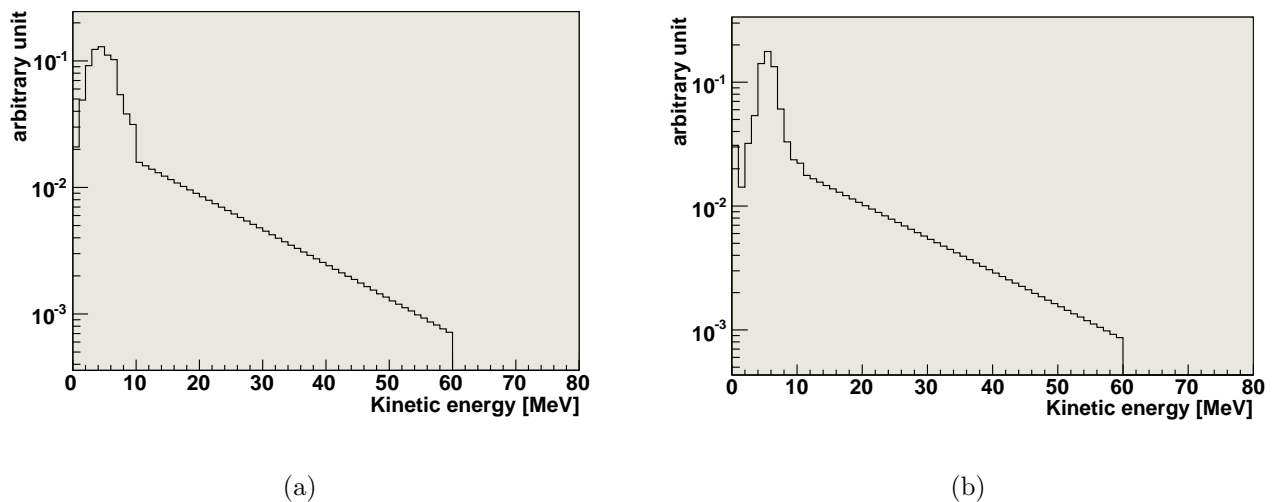

(a)

(b)

Figure 13: Neutron energy distributions obtained from Haoqi Lu [13]. Plots are normalized to unit integral. Spectra are for capture on carbon (a), and oxygen (b).

4.5   Neutron simulation

Neutrons were tracked until they stopped or left the water pool geometry, similar to the muon simulation. Thus, neutrons could be lost in two ways, they left the pool volume or took part in inelastic process with no secondary neutron emitted.

Overall, ∼6 million neutrons were generated, from which about 44% were captured. Almost all captures—more than 99.8%—were on hydrogen. Only 10 captures on gadolinium were recorded.

In fig. 14 the time distribution of capture is plotted. The mean value 194 μs approximately corresponds to the mean life time of neutron in water. Note that there are other materials in the water pool, as well as a thin layer of air above water, making a tail in the plotted dependency.

[†]Fraction of neutrons in the range 30–60 MeV is ≈13 times lower than in the range 0–60 MeV.
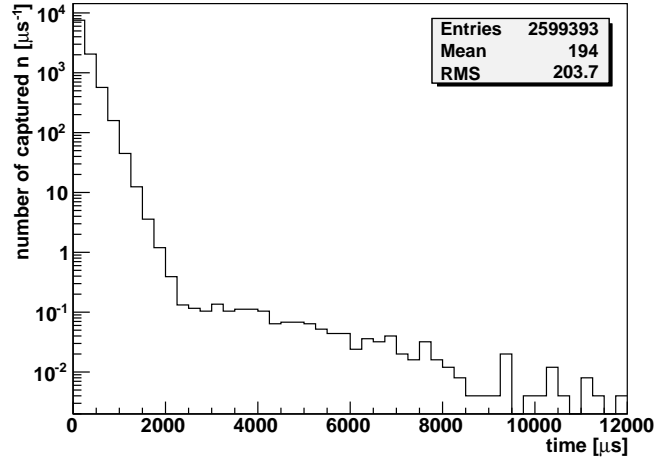
Figure 14: Time distribution of neutron capture.

(a)

(b)

(c)

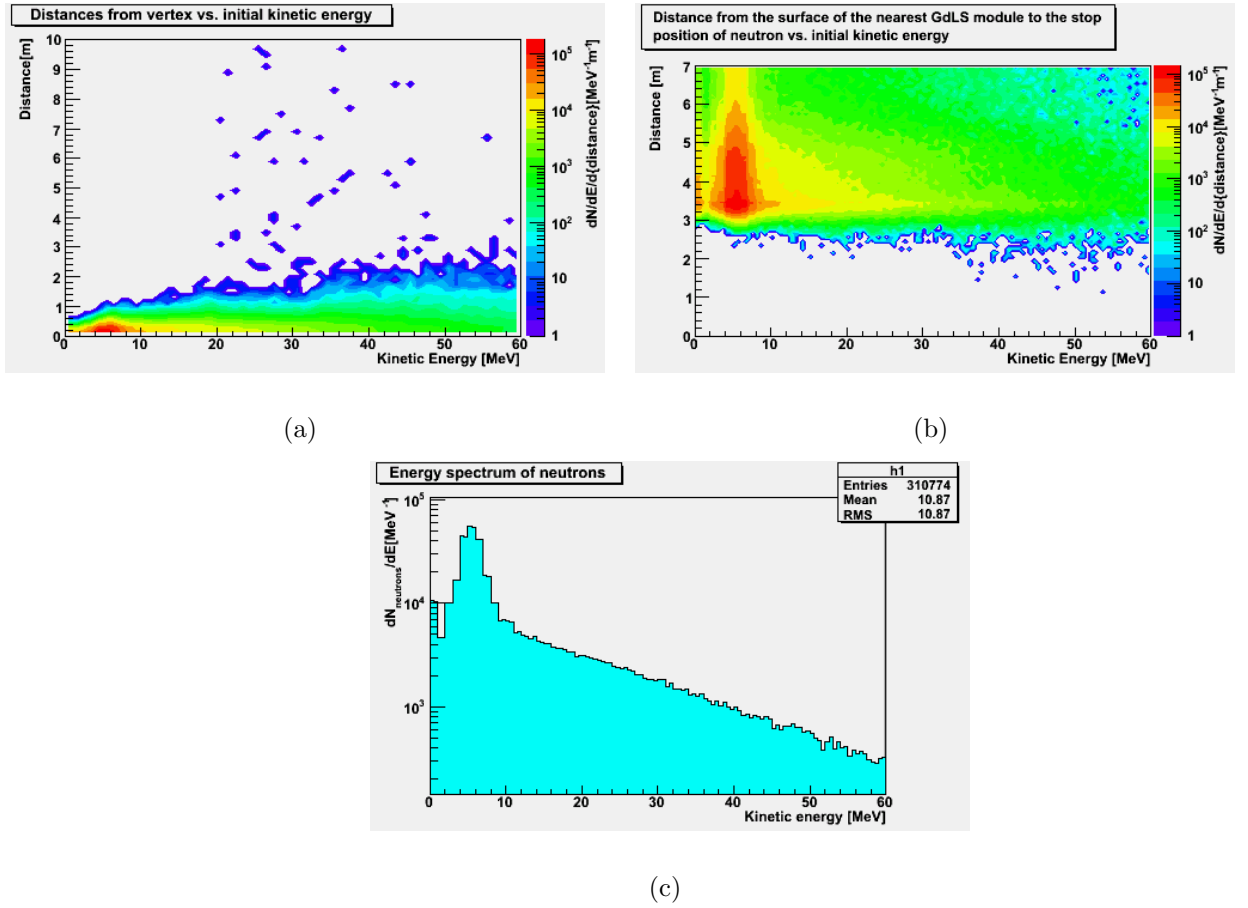**Figure 15:** (a)Distance between vertex position and stop position of neutron. There's visible change in dependency at 20MeV. But in figure of distances to the surface of the nearest GdLS vessel (b), there's no visible change. (c) Spectrum of neutrons.

4.6 Time calculation

To estimate the time corresponding to the simulation, the following equation was used,

$$T = f_{spec}N_{vertex}N_{\mu tot}S^{-1}\Phi^{-1} \tag{34}$$

25

where $f_{spec} \doteq 13$ is a factor which reflects the fact that neutrons were given energy from small range of their spectra, $N_{vertex} = 13$ is the number of neutrons generated in each vertex, $N_{\mu tot} = 3.3$ billion is total number of muons corresponding to the number of simulated ones. Φ is the muon flux, which was evaluated to be ≈ 0.041 m^{-2}s^{-1} for the far site (see section 3.7), and $S = 256$ m^2 is the surface of upper side of the pool, since most of the muons were generated from the top of the pool.

The result of 10 neutrons captured inside GdLS corresponds to the time roughly 1700 years.

4.7 Comparison

Haoqi Lu, one of the collaboration members, presented a study [13] on neutron production from μ^- capture. Unlike this work, he used G4dyb package with Geant4.7 for his simulation. All muons, which could be stopped inside water pool were simulated. In order to have some comparison, similar simulation work has been done. The upper energy limit 6.5 MeV was used for muon generation in [13]. Fig. 16 shows how the number of muons stopped inside the water pool depends on limiting energy. It can be seen, that the used limit was far enough from the beginning of plateau. For new calculations the same limit was used and number of μ^- simulated corresponds to 10 million of total muon number.

Since, in this work, other version of Geant4 was used, two simulations were performed using Geant4.8.1 and Geant4.8.2 packages respectively, to compare different implementations of μ^- capture process across the version Geant4.8.

Table 5 presents results from performed calculations, and compares them with work of Haoqi Lu. As a criterion of the comparison, the relative number of captures on particular elements was set. Another compared value was the ratio of stopped μ^- on particular element to all stopped μ^-. Data of Geant4.8.2 seems to be in a good agreement. However simulation using Geant4.8.1 differs. There were no neutrons emitted after μ^- stop on iron. Moreover, there is indication of a decrease in the capture rate for higher Z. This issue is discussed in appendix A.
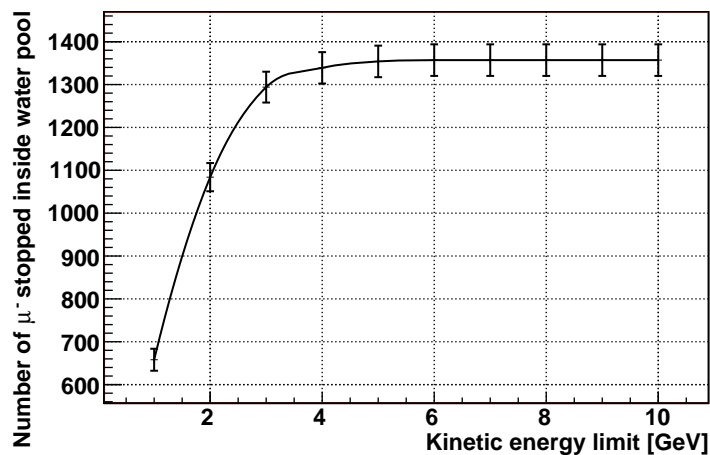

Figure 16: Number of μ^- stopped inside water pool versus energy limit.

Z:	stp.	cap.	cap./stp.	stp./all	*stp.	*cap.	*cap./stp.	*stp./all	**cap./stp.	**stp./all
1	35116	1	0.003%	29.44%	31975	0	0%	29.4%		29.4%
6	12789	976	7.6%	10.72%	14024	1040	7.4%	12.9%	8%	10.5%
8	69881	12521	17.9%	58.59%	61305	10513	17.1%	56.3%	18%	58.6%
26	989	911	92.1%	0.83%	1170	0	0%	1.1%	90.5%	0.9%
other	505	437	86.5%	0.42%	1747	236	13.5%	1.6%		0.6%

Table 5: Comparison with work in [13]. For nuclei of H, C, O, Fe with Z numbers 1, 6, 8, 26 respectively, there are number of μ^- stopped(stp.) on the nucleus, number of captured μ^-(cap.) with neutron emission, ratio of stopped to all simulated μ^-, and the ratio of captured to stopped. "*" denotes simulation with Geant4.8.1 G4MuonMinusCaptureAtRest process. The lower fraction of capture was caused by bugs inside Geant4.8.1 capture class. "**" labels data taken from [13]

5   Results & conclusions

Muon capture induced neutron background was simulated in two parts. First, muons were propagated through the water pool at the far site until they stopped. There were several limitations on these muons. Only μ^-s with kinetic energies under 300 MeV were tracked, and only until they left water pool or produced more than 1000 Cherenkov photons. For the simulation, Geant4 toolkit was used.

From 3.3 billion of muons, 458 thousands were captured with neutron emission in the water pool, satisfying the presented limitations.

From those positions, where muons stopped, 13 neutrons were generated. Only 10 neutrons got into the anti-neutrino module and captured on gadolinium. The time which corresponds to 3.3 billion of muons at far site is roughly 1700 years.

Such a low rate is a consequence of the water shield presence and reflects the fact how important is the water shielding for neutron background suppression. The result shows that this type of background is negligible.

During exploration of simulation softwares, Geant4 and G4dyb, a few mistakes in code was found and reported to corresponding developers. Thus, although the simulation code of Geant4 is very useful tool, its treatment of muon capture is not sufficient. In order to get better results, user has to do additional changes, e.g. change of neutron energy spectra.

Appendix

A MC simulation

Monte Carlo (MC) simulations, generally, use a Monte Carlo method to imitate real life or to make predictions in specific situations. The method is stochastic technique that is used to solve problems using random numbers and probability distributions. The task has commonly a very complex structure, which makes analytic solution impossible. Employing stochastic methods leads usually to the situation when one has to deal with a large number of iterations and to use a modern computer equipment.

The fundamental of the MC simulations is a random number generator. In practice, a truly random number generator can be used, however, this often requires an additional complicated hardware. It is more convenient to use the so called pseudo-random number generator, which is often software based algorithm producing random-like, pseudo-random, numbers.

In particle physics, the object of interest has essentially stochastic behavior. Most experiments require preliminary studies of a detector design and detailed analyses of the specific detector response. Here, the MC simulations represent a powerful tool.

For example, while tracking a particle, the algorithm have to decide, which process should be employed in particular moment. Each process has its own probability distribution, thus the algorithm randomly assign the particular probability to the corresponding process and then it randomly chooses between processes according to the assigned probability.

A.1 Geant4 simulation toolkit

Geant4 [15] is a programming toolkit used for simulating the passage of particles through matter, which provides a number of functionalities, like tracking, geometry, physics models, and hits, widely used in particle simulations.

The user is objected to write his own program utilizing the framework that Geant4 provides. There are few main components, that are necessary to incorporate to the program. User has to specify the fictive world, in which the simulation will take a part. This includes specification of volumes, e.g. detector parts, together with materials which they are made of. This is termed as geometry of simulation. Next, the user has to provide a list of processes to be involved in the simulation. This means, e.g., how a simulated particle can interact with matter or other particles.

Last thing, which is necessary for user to specify, is generation of initial particles. User can use prepared "generators"—the objects which prepare the initial particle and start the tracking—, or can make his/her own.

The random number generator, which Geant4 uses by default, is a part of CLHEP—A Class Library for High Energy Physics [16]—and employs an algorithm RANMAR which is specified in a review by F. James [17].

A.1.1 Capture of μ^-

This process is treated according to the scheme presented in the section 3.7.1. After the muon loses its kinetic energy and stops somwhere in material, an element is

randomly taken according to Fermi–Teller Z-law, which is described in [12]. Then it cascades down to the K-shell state, emitting photons. There, the algorithm chooses between decay of bounded muon or nuclear capture. When the nuclear capture is called, the center of mass system (CMS) energy of nucleus and muon is calculated. Difference between the CMS energy and nuclear mass is taken as available energy. Then a random proton is chosen from the nucleus and a collision with the muon is calculated with resulting neutrino, which escapes from the nucleus, and neutron. The neutron energy is then added to the excitation energy of a new nucleus which is consequently broken up.

The capture process of negatively charged muon has several problems in Geant4.8.1. The energy spectrum of emitted neutrons does not correspond to the measured one. In the study by Haoqi Lu [13], new neutron spectra are presented, resulting from experimental measurements [18, 19, 20].

Furthermore, after the muon captures on a nucleus, no neutrons are sometimes emitted although they are expected to.

After some look into the code of corresponding process, two main mistakes were found. First, there was a mistake in kinematics calculation, which led to a wrong energy of the system muon–nucleus. This slightly influenced the resulting energy distribution of secondary particles.

The second was a mistake in calculations of bounding energies of participating nuclei, leading to wrong excitation energy of the final state. Sometimes, the product nucleus had negative excitation energy which was assumed to be wrong. The nucleus was stated not to be excited and consequently, no neutrons were emitted.

The problem was reported to the CERN's developers of Geant4, and it was fixed for the version Geant4.8.2. However, the resulting energy spectrum of neutrons still remains different from the expected one, and it is assumed to be due to the simplified model of muon collision with the nucleus.

In fig. 17, distributions originating from both Geant4.8.1 and Geant4.8.2 are plotted. To check the change of the process, Geant4.8.2 muon capture was used in Geant4.8.1 too. For comparison, the spectrum from the work of Haoqi Lu is also presented. It is evident, that the spectrum from Geant4.8.1 has real deficit for higher energies. Spectra of Geant4.8.2 and Geant4.8.2 process in Geant4.8.1 does not differ significantly.

The table 5 shows the deficit of neutrons when Geant4.8.1 is used.

A.2 G4dyb package

G4dyb is a simulation software package which uses the Geant4 toolkit. It is developed by Daya Bay collaborators, and it provides a program to perform simulations. There are specified geometries of near and far sites, and user is allowed to choose between them. The package also contains tools for a simulation data collection and analyses.

A.2.1 Neutron–proton elastic scattering

The G4dyb program chooses which processes are considered for which particle. In this work, neutron propagation in the matter has a great importance since the goal is to estimate how many neutrons can be transported to the main detector.
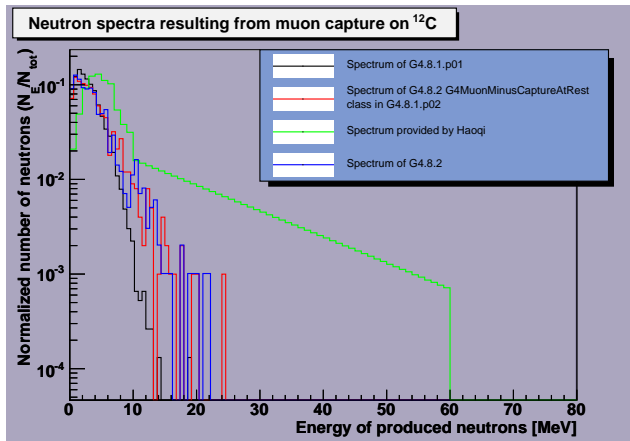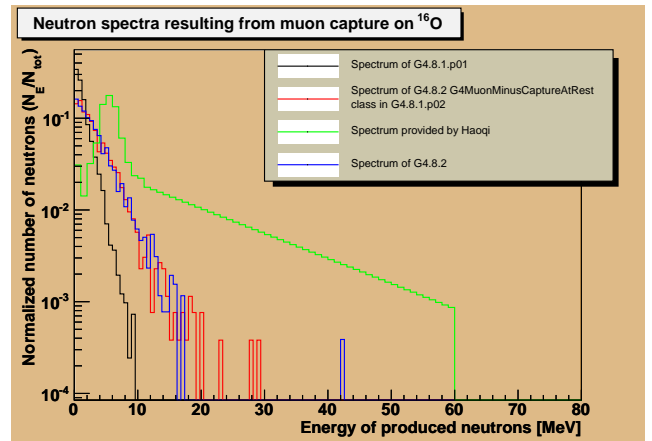
Figure 17: Comparison of neutron energy distributions as got using Geant4.8.1, Geant4.8.2 and their combination. The distribution provided from [13] is also added. All plots are normalized to unit integral. Spectra are for capture on carbon (a), and oxygen (b)

There appeared to be some problems with the process of elastic scattering of neutrons on protons when the kinetic energy of neutron was greater than 20 MeV. For lower energies a high precision model is used, while for energies above 20 MeV simpler and faster model is employed. Standard model—G4LElastic—, used for most hadrons' elastic scattering, often leads to loss of neutron when it gives all its energy to the proton. There is another model, G4LEnp, which should have fixed this problem. However, it was realized, that it behaves in a quite strange way. Geant4 applied it in elastic scattering on other elements although it was said not to.

Geant4 developers were contacted, and in response, a use of G4HadronElastic model was advised for the purpose of all elastic scattering processes of neutrons having kinetic energy above 20 MeV.

B   Cherenkov radiation

Cherenkov radiation is named after Pavel Alekseyevich Cherenkov who was the first to rigorously characterize it.

This radiation is emitted when a charged particle passes through an insulator at a speed greater than the speed of light in that medium. Particular photons form an acute angle with the particle direction. This angle can be obtained from basic calculations, which are similar to those of supersonic boom effect.

Suppose a particle with velocity $v > c/n$, where c is the speed of light and n is the refractive index of the insulator, moving from a point A at some initial moment $t = 0$. At a later time t time the particle travels a distance vt to a point B. The emitted electromagnetic waves, however, travel a distance ct/n from the point A. Thus, a wave front forms right triangle with a hypotenuse AB (see fig. 18). The angle ϑ can be easily expressed by

$$\cos\vartheta = \frac{c}{nv} = \frac{1}{n\beta}, \tag{35}$$
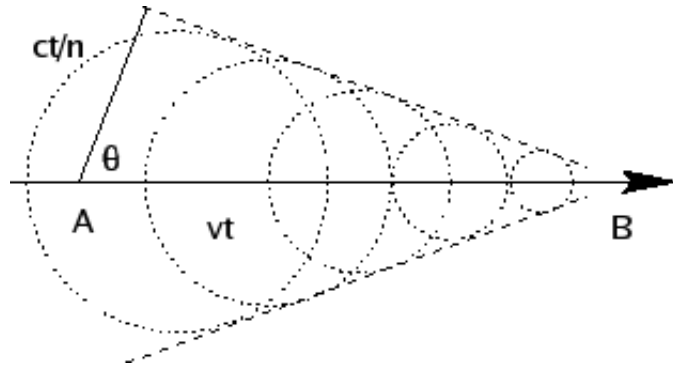
where β stands for dimensionless v/c.

Figure 18: Schematic chart of Cherenkov radiation by particle traveling with velocity v in material where the light propagate at speed $c/n < v$.

The number of photons dN with angular frequencies ranging from ω to $\omega + d\omega$ radiated on the path dx is described like[1]

$$\frac{dN}{dxd\omega} = \frac{q^2}{\hbar c^2}\left[1 - \frac{1}{\beta^2 n^2}\right] = \frac{q^2}{\hbar c^2}\sin^2\vartheta, \tag{36}$$

denoting $q^2 = e^2/4\pi\varepsilon_0$, where e is the electron charge and ε_0 is the electric constant. Note, that the index of refraction varies with the light wavelength, and that this relation is valid only for photons which satisfy $n(\omega) > 1/\beta$.

Now suppose radiation of photons from a frequency interval (ω_1, ω_2)—or in words of wavelength[2] (λ_2, λ_1)—where the refraction index is approximately constant. The energy loss due to this radiation on a unit path length is then

$$\frac{dE}{dx} = \frac{q^2}{c^2}\sin^2\theta\frac{1}{2}\left(\omega_2^2 - \omega_1^2\right) = (2\pi)^2 q^2 \sin^2\theta\frac{1}{2}\left(\frac{1}{\lambda_2^2} - \frac{1}{\lambda_1^2}\right), \tag{37}$$

---

[1]Derived from formula for particle's energy loss in material medium due to Cherenkov radiation as is in Paolo Budini's article [21]. This is an approximation for infinite track length of radiating particle.

[2]Note the well known relation $\omega = 2\pi c/\lambda$.

and the corresponding number of photons is

$$\frac{dN}{dx} = \frac{q^2}{\hbar c^2} \sin^2 \theta \frac{1}{2} (\omega_2 - \omega_1) = 2\pi \frac{q^2}{\hbar c} \sin^2 \theta \frac{1}{2} \left(\frac{1}{\lambda_2} - \frac{1}{\lambda_1} \right). \tag{38}$$

C   Photomultiplier tube—PMT

Photomultiplier tubes (PMTs) are detectors sensitive mainly to the light from a visible spectrum. They are frequently used for their exceptionally fast time response.

There's a scheme of PMT structure in fig. 19. It consists of evacuated tube with input window, photo-cathode, electron multiplier, and anode. High voltage (usually 1 to 2 kV) is applied on the photo-cathode and distributed by voltage divider to each dynode of the electron multiplier.

The light passes through the input window and excites electrons in the photo-cathode so that they are emitted into the vacuum—this is called external photoelectric effect. Photoelectrons are then accelerated and focused by the focusing electrode into the electron multiplier. This multiplier is a system of dynodes, specially designed electrodes which can emit more electrons from an incident one. After the accelerated photoelectrons land on the first dynode they kick out secondary electrons which are then accelerated onto the next dynode and so on. All secondary electrons from the last dynode are collected by the anode giving thus amplified signal.
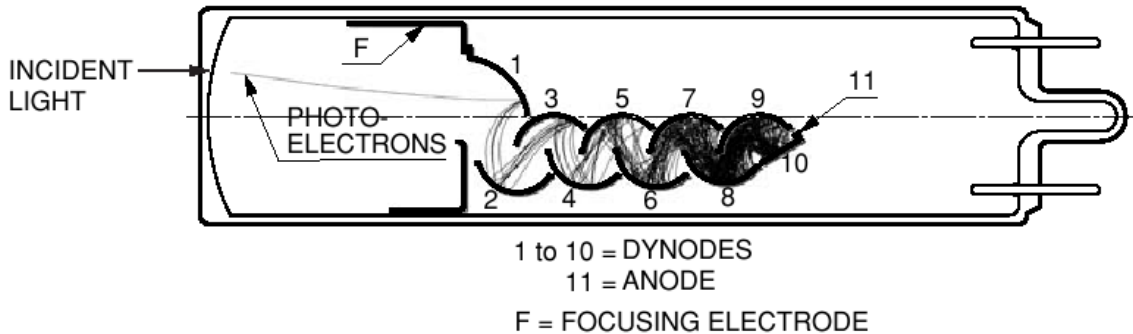

Figure 19: Schematic view of the so-called linear-focused PMT structure. The picture is taken from [22].

The process of photon conversion into photo-electron is a stochastic process. The probability that a photo-electron can escape from the photo-cathode when a photon strikes it is called quantum efficiency, and it varies with the photon wavelength. Since the electron excites through the energy of photon, the lower wavelength the photon has, the larger emission probability is. Thus a photo-cathode alone is more sensitive down to the ultraviolet region. However, the input window is usually not transparent for more energetic photons and tends to absorb the ultraviolet radiation. This determines the lower limit on the light wavelength.

Another characteristic that reflects spectral response of photo cathode is a radiant sensitivity, which is defined as the current of photoelectrons generated by photo-cathode divided by the incident radiant flux and expressed in units of amperes per watts (A/W).

Once the photo-electron is emitted, it doesn't necessarily need to be caught by the first dynode. Although dynodes are designed to modify trajectories of electrons so that they can be efficiently multiplied, some electrons may deviate and may not contribute to the multiplication. The probability of electron capture with secondaries emission is termed collection efficiency. This holds for all dynodes, but the effect becomes less and less significant from dynode to dynode.

The signal on the anode comes with time delay, which is due to the transport of the charge in the multiplier. This delay is called transit time. Electrons from the last dynode also arrive at a different time onto the anode, creating specific pulse shape on the output signal.

The transit time also varies from photon to photon, and the fluctuation is described by transit time spread.

In the Daya Bay experiment one of possible PMT types is R5912 manufactured by Hamamatsu Photonics. It is sensitive to the light of wavelengths from 300 nm to 650 nm. The radiant sensitivity is peaked at 420 nm. The transit time is 55 ns with spread 2.4 ns. The total gain from 10 dynodes of the multiplier is $\sim 10^7$.

Principles of PMT and description of its structure were taken from Hamamatsu's handbook [22], where the reader is referred to in order to get more detailed information. The parameters of R5912 type are from product's data sheet [23].

References

[1] E. Kh. Akhmedov *Neutrino physics*, arXiv:hep-ph/0001264v2.

[2] L. Wolfenstein, *Neutrino oscillations in matter*, Phys. Rev. D 17 p.2369 (1978)

[3] W.-M. Yao *et al.*, J. Phys. G 33, 1 (2006) and 2007 partial update for the 2008 edition available on the PDG WWW pages (URL: http://pdg.lbl.gov/).

[4] K. Anderson *et al. WHITE PAPER REPORT on Using Nuclear Reactors to Search for a value of θ_{13}* , arXiv:hep-ex/0402041v1.

[5] 'Recommendations to the Department of Energy and the National Science Foundation on a U.S. Program of Reactor- and Accelerator-based Neutrino Oscillation Experiments', http://www.science.doe.gov/hep/NuSAG2ndRptFeb2006.pdf.

[6] Daya Bay Experiment Conceptual Design Report (CDR), yet not available for public.

[7] C. Bemporad, G. Gratta, P. Vogel, *Reactor-based Neutrino Oscillation Experiments*, arXiv:hep-ph/0107277v1

[8] J. H. Manley, L. J. Haworth, and E. A. Luebke, *The Mean Life of Neutrons in Water and the Hydrogen Capture Cross Section* , Phys. Rev. 61, p.152 - 155 (1942).

[9] A. R. Ronzio, C. L. Cowan, Jr., and F. Reines, Rev. Sci. Instrum. 29, p. 146 (1958)

[10] X. Guo et al. (Daya Bay Collaboration), *A precision measurement of the neutrino mixing angle θ_{13} using reactor antineutrinos at Daya Bay*, arXiv:hep-ex/0701029, 2007. Proposal to DOE.

[11] T. Araki *et al.*, (KamLAND Collaboration), *Measurement of Neutrino Oscillation with KamLAND: Evidence of Spectral Distortion* Phys. Rev. Lett. 94, 081801 (2005).

[12] N.C. Mukhopadhyay, *Nuclear Muon capture*, Phys. Rep. 30 (1977) 1.

[13] Haoqi Lu *DYB-doc-535-v1*

[14] P. Antonioli, C. Ghetti, E. V. Korolkova, V. A. Kudryavtsev and G. Sartorelli, *A three-dimensional code for muon propagation through the rock: MUSIC*, Astropart. Phys. 7 (1997) p357 [arXiv:hep-ph/9705408].

[15] S. Agostinelli *et al.* [GEANT4 Collaboration], *GEANT4: A simulation toolkit*, Nucl. Instrum. Meth. A **506** (2003) 250.

[16] *CLHEP project web page*, http://proj-clhep.web.cern.ch/proj-clhep/

[17] F. James, *A review of pseudorandom number generators*, Comp. Phys. Comm. 60, p. 329 (1990).

[18] M. E. Plett and S. E. Sobottka, Phys. Rev. C 3, p. 1003(1971)

[19] T. Kozlowski *et al.*, Nuclear Physics A 436, p. 717 (1985)

[20] A. Van Der Schaaf *et al.*, Nuclear Physics A 408, p. 573 (1983)

[21] P. Budini, *Energy Loss and Čerenkov Radiation of a Relativistic Ionizing Particle*, Phys. Rev. 89, p. 1147 (1953).

[22] *Photomultiplier Tube Handbook*,
      http://sales.hamamatsu.com/assets/applications/ETD/pmt_handbook_complete.pdf

[23] *R5912 PMT data sheet*, http://sales.hamamatsu.com/assets/pdf/parts_R/R5912.pdf

[24] E. Kolbe, K. Langanke, and P. Vogel, *Muon capture, continuum random phase approximation, and in-medium renormalization of the axial-vector coupling constant*, Phys. Rev. C 50, 5, p. 2576–2581 (1994).

[25] B. Goulard and H. Primakoff, *Nuclear muon-capture sum rules and mean nuclear excitation energies*, Phys. Rev. C 10, 5, p.2034–2044 (1974)

[26] R.W. Huff, *Decay rate of bound muons*, Ann. Phys. 16, Issue 2, p. 288–317 (1961).

[27] lectures on *Principles of computational physics*, *Experimental methods of nuclear physics*, and *Experimental methods in subnuclear physics* at MFF CUNI in Prague.